Post-processing effects on microstructure, interlaminar and thermal properties of 3D printed continuous carbon fibre composites

C. Pascual-González[1], P. San Martín[1], I. Lizarralde[1,2,3], A. Fernández[1,4], A. León[1], C.S. Lopes[1,5], J. P. Fernández-Blázquez[1]

[1] *IMDEA Materials Institute, C/Eric Kandel 2, 28906, Getafe, Madrid, Spain.*

[2] *Hexcel Composites SL, c/ Bruselas 10-16, 28983, Parla, Madrid, Spain.*

[3] *Department of Materials Science, E.T.S. Ingenieros de Caminos, Polytechnic University of Madrid, 28040, Madrid, Spain.*

[4] *Materials Science and Engineering Department, University Carlos III of Madrid, Spain.*

[5] *Luxembourg Institute of Science and Technology, 5, Avenue des Hauts-Fourneaux, L-4362 Esch-sur-Alzette, Luxembourg*

Abstract

3D printing of continuous carbon fibre reinforced composites (CCFRC) based on fused filament fabrication (FFF) has a great potential for reproducing robust and complex geometries, generating little waste. However, 3D printed CCFRC present relatively poor interlaminar bonding and high void content in comparison to traditional composites. This work analyses the post-processing temperature effects on microstructure, interlaminar properties and thermal stability of the printed CCFRC. Treated pieces at 150°C showed a reduction of porosity by approximately 87% and improved interlaminar strength by 145%, without modifying nominal dimensions. In addition, the increase in T_g (from 109°C to 131°C) is ascribed to a drying effect during the post-processing, which reduces the plasticization of the treated parts and contributes to the general enhancement of mechanical properties of printed CCFRC coupons. The proposed post-processing moves this technology towards the development of functional composite components for high-performance structural applications.

---

*Corresponding author: cristina.pascual@imdea.org

Keywords: continuous carbon fibre reinforced composite, fused filament fabrication, porosity, post-processing, interlaminar properties

---

1. Introduction

Fused filament fabrication is the most widespread 3D printing technology, which permits to fabricate customised parts generating small amounts of waste material. The operational principle of this technology is based on a thermoplastic that is extruded through a nozzle in a viscous state at a certain temperature. Its temperature dramatically decreases in contact with the printing bed or previously printed layers, which causes the thermoplastic solidification. As a consequence, a volumetric contraction occurs, developing poor adhesion between layers and high porosity content in the printed pieces. Indeed, the state-of-the-art of FFF method put in evidence these detrimental effects on the mechanical properties of printed parts.[1–6]

The addition of continuous carbon fibres as reinforcement in the printing filament increases mechanical performance of the material. This technology allows to manufacture complex and highly customised functional components with a mechanical behaviour adapted to a concrete application, which are very difficult to be manufactured by conventional methods. The number of research publications reporting 3D printing of continuous fibre reinforced composites (CCFRC) with this technology has increased in the last years [7–21]. Nevertheless, the development of the composite 3D printing has yet to achieve maximum potential [22].

The mechanical properties of 3D printed CCFRC in longitudinal direction are equivalent than obtained for composites fabricated by traditional methods [23–25]. However, the response under transverse and interlaminar loads (normal and shear) is strongly influenced by the inherent defects of FFF method, attributed to an insufficient thermo-mechanical consolidation of the material during the deposition [26]. In fact, the effect of layer thickness [13], fibre volume content [13], printing parameters [27] and trajectories [28] on the interlaminar bonding performance of 3D printed continuous carbon, glass and Kevlar composites have been reported. Moreover, the calorimetric properties of the commercial printable materials of this technology hinder the correct adhesion between layers in comparison to other typical thermoplastics used in FFF technology [14], as well as the inhomogeneous fibre distribution in the microstructure may trigger premature failure of the materials [9, 14, 29]. It is clear from these statements, 3D printing of CCFRC requires further strategy to be considered a viable method for manufacturing high-performance structural parts [11, 26, 30].

Compaction stage seems to be the most adopted technique to post-process 3D printed CCFRC. The highest longitudinal tensile strength and modulus values were obtained after a compaction step at 200°C applying 200 kPa during 30 minutes [31]. Other investigation reported transverse tensile strength, flexural strength and Mode I interlaminar fracture toughness increased by 78%, 93% and 90% respectively by reducing to 6% in void content after hot-pressing at 230°C applying a pressure of 5 MPa during 10 minutes [32]. However, to combine 3D printing with high-temperature and high-pressure is impractical to retain the geometry of nominal design. Other approaches have been: (i) the chemical treatment, which increased by 12% the tensile property of carbon reinforced PLA composites [33], (ii) the assemble of a hot-compactation roller to a FFF 3D printer, obtaining similar bending properties as the hot-pressed specimens [34], and (iii) the vacuum annealing [35].

This work proposes an optimised post-processing, demonstrating its feasibility to minimise the void content after 3D printing without affecting nominal dimensions of the printed coupons. The effects of different temperatures on the microstructure, interlaminar and thermal properties are investigated.

2. Experimental methods

2.1. 3D printer, materials and manufacturing constrains

The specimens analysed in this study were fabricated using a commercial FFF 3D printer of CCFRC (Markforged, model: MarkTwo). This printer has two extrusion systems, one for printing neat Nylon (Polyamide 6, abbreviated as PA6) and the other for printing reinforced material, which consists on continuous carbon fibres (CCF) embedded into polymer matrix (amorphous Polyamide, abbreviated as PA) [14]. This technology presents the following manufacturing constrains: (i) fixed printing parameters, such as extrusion temperature, printing speed and layer thickness; (ii) restricted printable materials; (iii) the impossibility of printing only reinforced material. Indeed, PA6 contours, roof and floor layers are added in all specimen by default. Figure 1 shows a schematic representation of printed material configuration. Worth to be highlighted the polyamide of thermoplastic matrix embedding the CCF (PA) and the unreinforced material (PA6) covering is not the same.

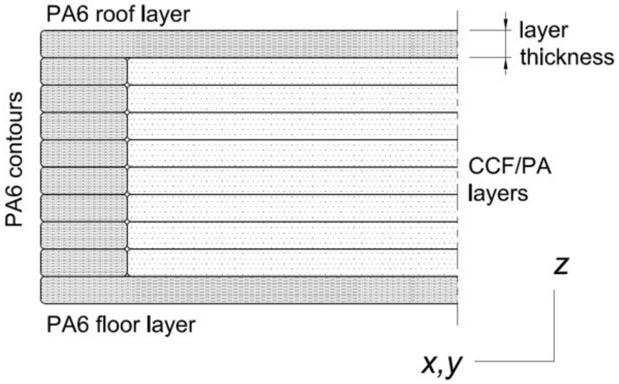

Figure 1: Schematic representation of manufacturing specimen constrain. The semi-crystaline Nylon (PA6) contours, roof and floor layers always cover continuous carbon fibres reinforced amorphous polyamide (CCF/PA) composite.

Consequently, the calorimetric properties of both polyamides have to be considered to select the post-processing temperatures.

2.2. Heat treatment optimisation

Post-processing temperatures were determined from thermal characterisation of printable materials (PA6 and CCF/PA) which was performed using a differential scanning calorimeter (DSC, model Q200, TA Instruments) up to 300°C with a heating rate of 10°C/min. One unidirectional CCFRC with dimensions 105 mm x 28 mm x 2.5 mm was printed for each treatment condition and post-processed in the hot plates (Fortine PressesR®) at different temperatures during 15 minutes (heating speed of 10°C/min) applying 3 kN, which is the minimum operational force to ensure the temperature is held constant in all the sample. The pressure applied was 1 MPa, which is in the same order of magnitude of other composite manufacturing methods, such as autoclave [36]. The automated C-Scan ultrasonic scanning (TRITON 1500, Tecnitest) was used to monitor internal defects in treated samples. Porosity content and failure mechanisms of short beam test specimens were determined through the analysis of the results obtained by X-ray computed micro-tomography, using a General Electric Phoenix Nanotom 160 kV. The target was molybdenum, 0-mode nanofocus and no additional filter materials were used. The voltage of the X-ray tube for the scan was 50 kV and the current was 200 µA.

2.3. Mechanical characterisation of 3D printed CCFRC

Interlaminar response characterisation of 3D printed CCFRC was carried out according to ASTM D 2344 [37]. The sample dimensions for the Short Beam Shear test were determined on the basis of the final thickness after the post-processing. The sample length and width were six and two times its thickness, respectively. The tests were carried out in an electromechanical machine (Instron 3384) with a 5 kN load cell at a loading speed of 1 mm/min. The interlaminar shear strength (ILSS) was calculated using the following expression 1, which defines the maximum shear stress:

$$ILSS = 0.75 \cdot \frac{P_m}{b \cdot h} \tag{1}$$

where P_m is the maximum load, b and h are the sample width and thickness.

Dynamic mechanical analysis (Q800, TA Instruments) was used to examine thermo-mechanical behaviour with single cantilever clamp. Unidirectional printed samples of thickness ranging from 2.15 mm to 2.75 mm (depending of the treatment temperature), were cutted into approximate 30 mm x 10 mm rectangles and heated from -100°C to 230°C with a heating rate of 3°C/min. Samples of 5 mg were taken from unreinforced material (PA6), CCF/PA composite and treated specimens to study thermodynamic phenomena using Q200 differential scanning calorimeter (TA Instruments) from room temperature up to 300°C with a heating rate of 10°C/min. TGA equipment (Q50, TA Instruments) was used to evaluate the thermal stability and water content of treated specimens up to 1000°C, analysing the weight variation as a function of the temperature in air atmosphere.

3. Experimental results and discussions

DSC heating curves for unreinforced Nylon (PA6) and CCF/PA composite are shown in Figure 2, which are the raw materials used for printing the specimens examined in this work. First heating curves exhibit broad exothermic peaks at 100°C attributed to water evaporation (indicated by arrows in Figure 2 (a)), being the unique thermal transition observed in amorphous PA. The first transition for semi-crystalline nylon (PA6) appears around 40°C, corresponding to the glass transition (T_{g1}) of PA6 (black curve in Figure 2 (a)). As temperature increases, melting point is reached at 198°C (T_m, peak 2 in Figure, 2 (a)). Both values are in agreement with literature

[38]. The second heating curve for PA6 reveals a shoulder at lower temperatures of the melting point (peak 3 in Figure 2 (b)), also previously informed [39]. On the other hand, DSC profile of CCF/PA composite (red curve in Figure 2) indicates totally amorphous polymer with a glass transition at 130°C (Tg_2, peak 4 in Figure 2 (b)). The post-processing temperatures were chosen based on these calorimetric properties of constituent materials: (i) at 70°C, between T_{g1} and T_{g2}; (ii) at 130°C, corresponding to T_{g2}; (iii) at 150°C, between T_{g2} and T_m; (iii) at 170°C, slightly below T_m; (iv) at 210°C, slightly above T_m; (v) at 230°C, between T_m and the printing temperature; and (iv) at 250°C and at 270°C, in the range of the printing temperatures of PA6 and CCF/PA.

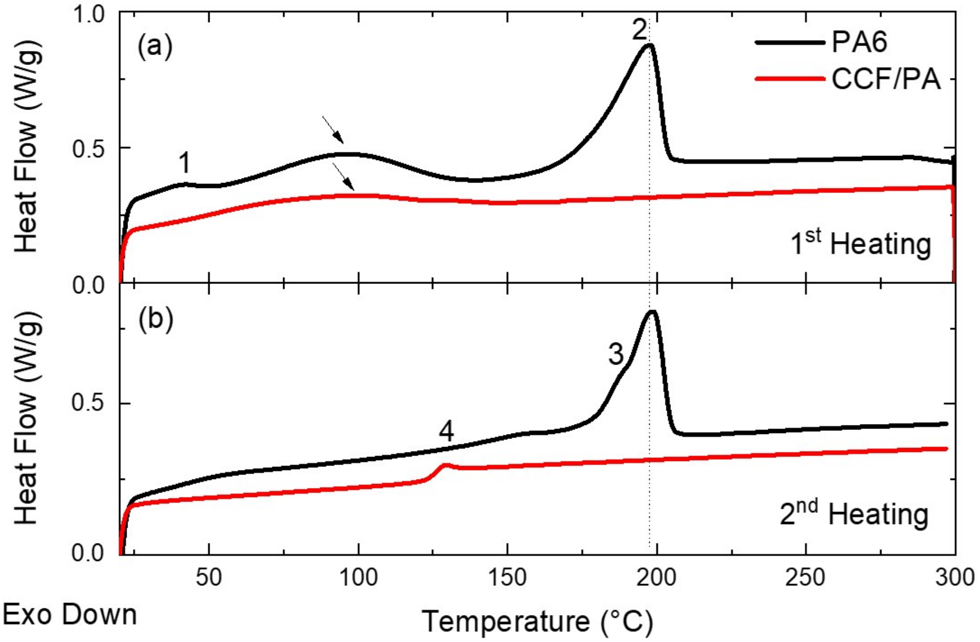

Figure 2: (a) First and (b) second DSC heating curves applied to semi-crystaline Nylon (PA6, black curve) and continuous carbon fibres reinforced amorphous polyamide (CCF/PA, red curve) composite from room temperature to 300°C. Scanning rate: 10°C/min

Then, nine rectangle shaped coupons of unidirectional CCFRC with dimensions 105 mm x 28 mm x 2.5 mm were printed for the experimental procedure. Table 1 shows the variation of coupons length, width and thick-

Table 1: Dimensions and variation of coupons length, width and thickness after 3D printing and after heat treatment compared with nominal model.

	After 3D printing						After post-processing					
	Dimensions (mm)			Variation (%)			Dimensions (mm)			Variation (%)		
Temperature (ºC)	**Length**	**Width**	**Thickness**	**Length**	**Width**	**Thickness**	**Length**	**Width**	**Thickness**	**Length**	**Width**	**Thickness**
Untreated	104.85	27.91	2.75	-0.14	-0.32	10.00	-			-		
70	104.71	27.93	2.74	-0.28	-0.25	9.60	No variation			No variation		
130	104.60	27.97	2.81	-0.38	-0.11	12.40	105.31	28.36	2.51	0.68	1.39	-10.68
150	104.60	27.94	2.79	-0.38	-0.21	11.60	104.66	29.25	2.46	0.06	4.69	-11.83
170	104.47	27.94	2.75	-0.50	-0.21	10.00	105.41	29.81	2.31	0.90	6.69	-16.00
210	104.57	27.94	2.78	-0.41	-0.21	11.20	108.97	30.64	2.16	4.21	9.66	-22.30
230	104.58	27.93	2.78	-0.40	-0.25	11.20	109.13	30.39	1.97	3.52	8.27	-29.14
250	104.89	27.92	2.78	-0.10	-0.30	11.20	110.05	33.25	1.84	4.70	21.88	-33.81
270	104.87	27.95	2.75	-0.12	-0.18	10.00	Failed post-processing			Failed post-processing		
			Average	-0.30 ±0.15	-0.23 ±0.06	10.80 ±0.94						

ness after 3D printing and after heat treatment. The dimensions of printed coupons in the xy plane (length and width) were undersized compared to the nominal model, around (0.30±0.15)% and (0.23±0.06)%, respectively. This phenomenon is inherent in the 3D printing process, as the fused filament shrinks when coming in contact with the printing bed [40, 41]. On the other hand, the dimension in the z direction (thickness) was oversized. An average error of 10.80±0.94% in comparison with the 3D model was obtained. This error seems to be higher than reported for others desktop 3D printers, which is usually kept about three to four times higher than the average error for each dimension in the xy plane [40, 42]. This remarkable thickness error can be hypothetically attributed to the difficulty of depositing a continuous carbon fibre filament. In overall, these results are consistent with other studies that have evaluated the dimensional accuracy of 3D printed composite parts [43, 44]. Table 1 also contains the dimensional coupon change after post-processing at 70°C, at 130°C, at 150°C, at 170°C, at 230°C and at 250°C. The dimensions of coupon treated at 270°C are not included because the post-processing failed. The coupons thickness decreased continuously with increasing temperature, to a maximum reduction of 1.8 mm for 250°C. As expected, this tendency is accompanied by a systematic growth in the other two dimensions. However, worth to be mentioned the thickness reduction of approximately 10% after post-processing compensates the deviation observed in z direction after 3D printing. Indeed, Figure 3, which shows the dimensional variation between the nominal design and the after post-processing parts, confirms the dimension of the samples treated at 130°C and 150°C were closer to the nominal 3D model than the untreated.

Figure 4(a) shows the C-Scan ultrasonic images for the unidirectional CCFRC coupons untreated (UT) and treated at different temperatures. The color scale represents relative response of the ultrasonic energy attenuation,

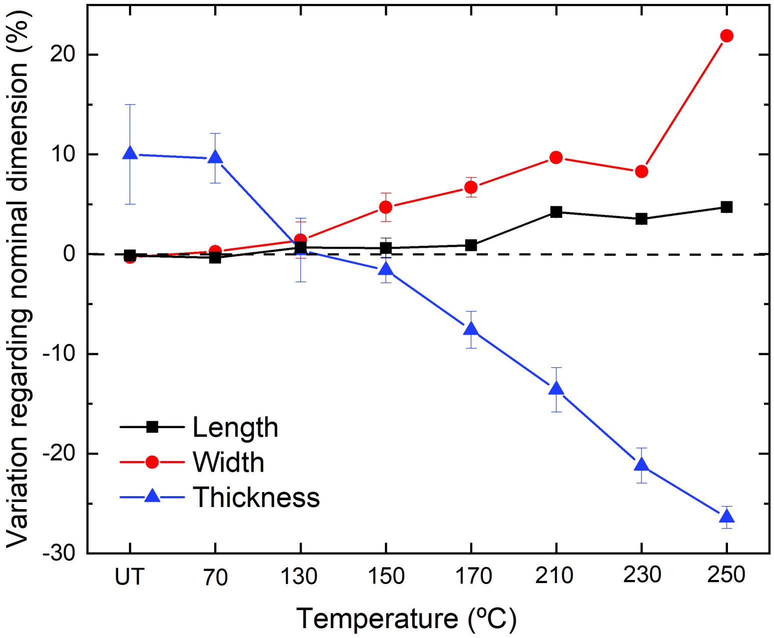

Figure 3: The dimensional variation between the nominal design and the after post-processing parts at different temperatures (70°C, 150°C, 170°C, 230°C and 250°C).

as shown accompanying scale. Attenuation level less than 6 dB are displayed in dark blue and it is considered homogeneous and defect free composite. Overall, void content decrease with increasing post-processing temperature. The ultrasonic wave was totally attenuated (over 30 dB) during the inspection of untreated and treated at 70°C coupons, suggesting a complete deconsolidation between the deposited layers with a large amount of entrapped air inside. 3D printed CCFRC coupons treated at 130°C, at 150°C and 170°C represent intermediate cases with areas with different levels of attenuation. In the C-scan of treated coupon at 130°C, the attenuation increases from the centre to the edges, indicating the entrapped air is moving towards these regions. The central area of treated coupons at 150°C and at 170°C were properly consolidated, although there is still remarkable entrapped air accumulated near the edges. Appropriate consolidation (attenuation below 6 dB) is observed in the coupon treated at 210°C. Even if C-scans images of specimens treated at 230°C, 250°C and 270°C indicated that most of the areas were well consolidated, some defects could be distinguished, probably associated with fibre displacement or matrix bleeding. Literature reports the air located in the centre of the conventional composite laminates is the most difficult to remove [45, 46]. These results suggest opposite, indicating 3D printing creates more defects in the perimeter than specimens manufactured by hot compression moulding. Indeed, on the edges is where the deposition turn, which leads the creation of airgaps between printing tracks [7]. Figure 4(b) shows failed post-processing at 270°C (on the top) in comparison with untreated piece (on the bottom). The material completely flowed during the treatment, which caused the loss coupon shape.

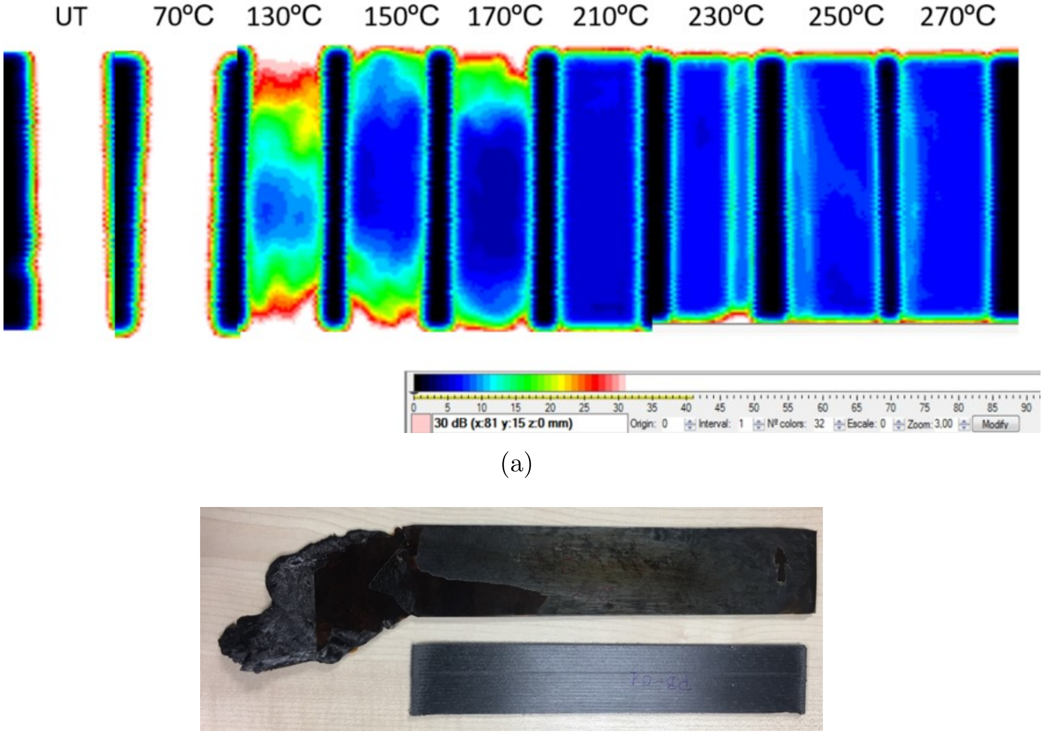

(a)

(b)

Figure 4: (a) C-Scan ultrasonic images for the unidirectional CCFRC coupons untreated (UT) and treated at 70°C, at 130°C, at 150°C, at 170°C, at 230°, at 250°C and at 270°C. Color spectrum of the dB losses in the bottom. (b) Failure post-processing at 270°C. Untreated sample also shown on the bottom.

Quantitative porosity analysis of 3D printed coupons was performed extracting the data from the volumes obtained by means of X-Ray Computed

Micro-Tomography (X-CT). The material-air threshold for image segmentation was manually selected, based on the difference in X-Ray absorption between the composite part itself and the entrapped air. After this binarisation step, the total porosity of the volume was rendered with the 3D image analysis software MeshLab. In addition, void content was finally calculated by analysing each volume using Python. Figure 5(a) shows the evolution of porosity as a function of temperature. Untreated coupon contains a voids volume fraction of 7.5%, which is similar than reported in literature [10, 11, 30, 47, 48]. Slightly higher value is obtained for treated part at 70°C, this may be associated with the variability of voids content within the same coupon, as observed in C-Scan images (Figure 4(a)). Porosity decreases with temperature up to approximately 0% for 250°C. The greatest reduction (87%) is observed between 130°C and 170°C, where PA (inner matrix) glass transition is overpassed without reaching the melting point of Nylon skin. The average void content in this temperature range is 1.1%. For higher temperatures was not possible to retain the shape of 3D printed unidirectional CCFRC coupons, as noticed in Table 1. Moreover, some defects start to appear when samples are treated above 230°C, as previously commented. Figures 5(b) and 5(c) show 3D rendering of the voids present in the full volumes of untreated and treated at 70°C 3D printed composites. In both images are indicated the bottom and the top layers, which corresponds the first and the last layers that were deposited during the printing process, respectively. Although these samples have similar void content values, the voids shape, size and distribution are completely different. As can be noted from the images, voids are generally accumulated along fibre direction and have an elongated shape. However, untreated coupon presents a void gradient along z direction (Figure 5(b)). In addition, larger and rounded shaped voids are distinguished in the last printed (top) layers. Probably this is because these layers experienced less heating cycles than the bottom layers, leading the formation of these types of defects. In other words, deposited material heats the bottom layers sufficiently to obtain a better thermo-consolidation [26, 49]. The voids are located between layers and traces but not within the filaments, as previously informed [14]. The post-processing at 70°C did not reduce the porosity of 3D printed composite but homogenised the distribution of voids.

The experimental strain-stress curves under short-beam three point bending load for the unidirectional CCFRC coupons untreated (UT) and treated at 70°C, at 130°C, at 150°C, at 170°C, at 210°C, at 230°C and at 250°C are shown in Figure 6 (a)-(h). The mechanical response achieved is highly dependent of the post-processing temperature. Interlaminar shear strength (ILSS) increases with temperature up to 210°C, indicating interlaminar bonding is consolidating. Different trend is observed for temperatures above 210°C, where mechanical response slightly decreases.

The modulus and the ILSS values of untreated coupon were 371 MPa and 31 MPa. The maximum increase of these variables occurs at 150°C accordingly with maximum porosity reduction. The modulus and the ILSS values at this point were improved about 89% and 145% in comparison with untreated sample, corresponding to 702 MPa and 76 MPa. However, the maximum values of 777 MPa and 84 MPa were obtained at 210°C. Worth to be mentioned that desired failure modes were not obtained only. In general, significant inelastic deformation and ductile behaviour were observed in all parts tested. Dominant Shear failure mode was only obtained for untreated and treated at 70°C parts, as shown in Figure (7(a)). Failure modes became more complex with increasing temperature. Apart from the small delaminations, additional tension and compression failure modes were identified in coupons treated above 150°C, as shown in Figure (7(b)). Moreover, a positive effect on the mechanical response can be associated with the increases of fibre volume fraction, which varies from ∼25% (UT coupon) up to ∼30% (coupon treated at 230°C). The fibre volume fraction values were calculated based on the coupon dimensions after post-processing and the experimental fibre content within CCF/PA filament, which is ∼35%.[14] Figure 8 shows the evolution of ILSS and fibre volume fraction values with temperature. Both magnitudes follow the same tendency with increasing temperature. However, coupon treated at 150°C, which has similar fibre volume fraction and porosity than the part treated at 130°C (Figure 8), presents significantly higher interlaminar properties than this last (from 50 MPa to 76 MPa). In this case, other factors are key on the enhancement of mechanical performance and they will be discussed later.

Figure 9 shows DMA curves from -100°C to 180°C. Three distinct regions are distinguished, reflected as peaks on the tanα curves (Figure 9 bottom) and as downward steps in the storage modulus curves (Figure 9 top), corresponding to: (i) β-relaxations probably for both polyamides, semicrystalline and amorphous (indicated in Figure 9 as β_{PA6} and β_{PA}), (ii) α and α'-relaxation for PA6 (α_{PA6} and α'_{PA6}) and (iii) α-relaxation for amorphous PA (α_{PA}), in order of increasing temperature.

The β transition occurs between -60°C and -70°C typically attributed to non-hydrogen-bonded amide groups [50] and more specifically to water bound on carbonyl groups [51]. This relaxation has been previously observed in both polyamides, PA6 and PA [14]. This relaxation remains unaffected by the post-processing temperatures. The α-relaxation at ∼30°C and the shoulder at higher temperature due to α' -relaxation coincide with reported DMA curves for PA6 and Onyx (commercial filaments used for this technology, [14]). These mechanical relaxations (α_{PA6} and α'_{PA6} in Figure 9) exhibit more variability with post-processing temperature, but it is not possible to determine a tendency. Indeed, these events are not well defined may be due to the amorphous nature of the PA matrix [52]. The PA6 is just presented in the skin of the printed samples (Figure 1).

Finally, the remarkable α-relaxation for amorphous PA on the tan α curves, which is attributed to hydrogen-bonded amide groups in the amorphous regions of the inner of the printed material [51], determines the glass transition (T_g) of the unidirectional CCFRC coupons. The T_g varies from 109°C to 131°C with increasing post-processing temperature. It is well known that the position of α-relaxation is highly influenced by the absorbed water in polyamides [53, 54]. Therefore, the drastic increase in T_g can be hypothetically ascribed to a drying effect during the post-processing, which reduces the plasticization of the treated parts. A similar trend has been reported for other PA-based composites exposed to moisture [50, 55–57]. The experimental relaxation intensity decreases with increasing post-processing temperature, in agreement with reported in literature [55]. On the other hand, the storage modulus systematically increases with post-processing temperature, excluding the coupon treated at 210°C. The storage moduli at room temperature for the post-processed sample at 170°C is 42% higher than the UT sample. This behaviour also supports the hypothesis of the occurrence of a drying effect during the post-processing. Indeed, similar tendency has been previously observed for PA6/clay nanocomposites [55].

From DMA results is derived the hypothesis that the higher is post-processing temperature, the lower is the water absorbed by the matrix of CCFRC, leading the increase of T_g values and contributing to the general enhancement of mechanical properties of printed CCFRC coupons. The commercial materials used in this technology have a considerable quantity of water absorbed from factory, up to 8% of its weight [14]. May be this is due to the plasticizer effect of the absorbed water on the polyamide which facilitates the printability of these CCFRC. Once, the printed parts are post-processed the water is not reabsorbed from the environment. The systematical shift of α-relaxation towards higher temperatures suggests there should be a relation between the quantity of absorbed water and the post-processing temperature. This point is examined by the TGA and DSC experiments.

Figure 10 shows the TGA curves of the CCFRC coupons untreated (UT) and treated at 70°C, at 130°C, at 150°C, at 170°C and at 210°C. The inset graph of Figure 10 reveals the weight loss in the temperature range associated to the water evaporation since UT sample to post-processed at 210°C. The reduction of weight loss from 2.3% to practically 0% for samples treated at 170°C and 210°C, corroborates the drying effects, reducing the plasticizer effect of water and consequently, the increase of the T_g discussed above. No more systematic variations were found at higher temperatures. All samples showed three additional degradation steps (Figure 10): (i) degradation starts at 400°C and reach the maximum weight loss at $\sim$460°C; (ii) a second degradation step is observed at $\sim$550°C (both processes are associated to polyamide degradation [14]); (iii) finally, the step at 770°C is due to carbon fibre decomposition.

The effect of the water content in the printed CCFRC coupons untreated (UT) and postprocessed is also observed in DSC thermograms on Figure 11. The samples UT and treated at low temperatures (130°C and 150°C) show an endothermic peak between 100°C and 150°C due to water evaporation (narrowed on Figure 11). The intensity of this peak decreases with post-processing temperature, which is still presented in sample treated at 150°C, and negligible for treatment above 170°C.

The T_g is overlapped to this water evaporation peak at lower temperatures and increases progressively from 54°C for UT sample to 103°C for treated at 210°C (marked by * on Figure 11). Therefore, the drying effect during post-processing is also confirmed by DSC, reducing the plastification of water and increasing T_g.

Worth to be noted the variation in the melting endothermic peaks sequence with post-processing temperature. All samples present a melting peak at 203°C (marked by a dashed line on Figure 11), being the unique melting peak observed for UT sample. Upon post-processing temperature, new peaks emerge at lower and higher temperatures. The sample treated at 130°C showed a peak at 169°C (marked by 1 on Figure 11) and small one at 247°C (marked by 2 on Figure 11). The sample post-processed at 150°C, has an overlapped shoulder to the peak at 203°C, centered at 192°C (marked by 3 on Figure 11), and a peak at 231°C with higher melting enthalpy (marked by 4 on Figure 11). The samples post-processed above 150°C present extra peaks at higher temperatures (marked by a solid line on Figure 11). Post-processing temperatures were higher than T_g, that produced cold crystallization in all samples, with new crystal phases which melted at temperatures 40°C higher than post-processed samples. This fact provided an increase of crystallinity, not quantified due to the difficulty of integrating melting peaks in thermograms where base line is not clear, but there are no doubts about this rise as it is observed Figure 11. However, it is worth to mention additional crystallisation is not observed in UT sample because of the rapid cooling of the material during 3D printing (Figure 6(c)). The increase of crystallinity during post-processing could have an effect in the mechanical properties, increasing for example elastic modulus. But, taking into account that PA6, responsible of this crystallisation, is part only of the skin, and the core is formed by CF/PA composite. Therefore, low influence of PA6 crystallinity in the mechanical properties of 3D samples is expected. More studies about the influence of cold crystallization during thermal treatment in final properties of composites will perform in near future.

4. Summary and Conclusions

The post-processing effects on the mechanical response, microstructure and thermal stability of 3D printed unidirectional CCFRC coupons were characterised in order to overcome the typical drawbacks attributed to FFF. CCFRC coupons were post-processed in the hot plates at different temperatures (70°C, 130°C, 150°C, 170°C, 210°C, 230°C, 250°C and 270°C) during 15 minutes applying 1 MPa. From the results presented in this work is derived the optimum post-processing temperature is 150°C, considering the dimension accuracy, the microstructure, thermal and mechanical properties of the final parts.

First, post-processing corrected the 10% deviation in z direction after 3D printing, attributed to the difficulty of depositing continuous carbon fibre.

Second, C-scan images show the central region of treated CCFRC coupons at 150°C and at 170°C starts being well consolidated, but entrapped air was still remained in the edges.

Third, X-CT results reveal the porosity is eliminated for post-processing temperature above 210°C. However, the greatest reduction (87%) is observed between 130°C and 170°C, corresponding to the maximum void reduction.

Fourth, the glass transition (T_g) of the unidirectional CCFRC coupons varies from 109°C to 131°C with increasing post-processing temperature. This significant increase in T_g is assigned to a drying effect during the post-processing, which is demonstrated to reduce the plasticization of the treated parts. Moreover, the appearance of higher crystallinity during post-processing could have a positive effect on the mechanical performance of printed CCFRC coupons.

Overall, this work has proposed an optimised post-processing for 3D printed CCFR with the aim of reaching a compromise among different aspects: (i) dimensional changes, (ii) void content, (iii) interlaminar shear strength and (iv) moisture content. Including this post-processing to FFF method to print CCFRP will promote this technology to be considered viable for high-performance structural applications.

Acknowledgements

This paper is dedicated to the memory of Dr. Claudio S. Lopes, who recently passed away. I would like to express my gratitude for giving me the opportunity to work in Spain, and I will never forget. He was not only a brilliant scientist, he was an inspiring leader and a good friend.

The research leading to this publication received financial support of the Spanish Ministry of Science and Innovation through project ADDICOMP (grant RTI2018-094435-B-C33). C. Pascual-González acknowledges financial support of the *Sistema Nacional de Garantía Juvenil* from the Autonomous Community of Madrid (grant PEJD-2017-POST/IND-4401). A. Fernández acknowledges the FPU grant (FPU16/02223) supported by the Spanish Ministry of Education, Culture and Sports.

References

[1] A. P. V. Puerta, S. Fernandez-Vidal, M. Batista, F. Girot, Fused deposition modelling interfacial and interlayer bonding in pla post-processed parts, Rapid Prototyping Journal (2019).

[2] M. Domingo-Espin, J. M. Puigoriol-Forcada, A.-A. Garcia-Granada, J. Llumà, S. Borros, G. Reyes, Mechanical property characterization and simulation of fused deposition modeling polycarbonate parts, Materials & Design 83 (2015) 670–677.

[3] J. Wang, H. Xie, Z. Weng, T. Senthil, L. Wu, A novel approach to improve mechanical properties of parts fabricated by fused deposition modeling, Materials & Design 105 (2016) 152–159.

[4] Q. Sun, G. Rizvi, C. Bellehumeur, P. Gu, Effect of processing conditions on the bonding quality of fdm polymer filaments, Rapid Prototyping Journal (2008).

[5] D. Qiu, N. A. Langrana, Void eliminating toolpath for extrusion-based multi-material layered manufacturing, Rapid prototyping journal (2002).

[6] A. Kantaros, D. Karalekas, Fiber bragg grating based investigation of residual strains in abs parts fabricated by fused deposition modeling process, Materials & Design 50 (2013) 44–50.

[7] L. Blok, M. Longana, H. Yu, B. Woods, An investigation into 3D printing of fibre reinforced thermoplastic composites, Additive Manufacturing (2018). URL: `http://linkinghub.elsevier.com/retrieve/pii/S2214860417305687`. doi:10.1016/j.addma.2018.04.039.

[8] A. N. Dickson, J. N. Barry, K. A. McDonnell, D. P. Dowling, Fabrication of continuous carbon, glass and Kevlar fibre reinforced polymer composites using additive manufacturing, Additive Manufacturing 16 (2017) 146–152. URL: `http://dx.doi.org/10.1016/j.addma.2017.06.004`. doi:10.1016/j.addma.2017.06.004.

[9] M. J. John, S. Thomas, Biofibres and biocomposites, Carbohydrate polymers 71 (2008) 343–364.

[10] F. V. Der Klift, Y. Koga, A. Todoroki, M. Ueda, Y. Hirano, R. Matsuzaki, 3D Printing of Continuous Carbon Fibre Reinforced Thermo-Plastic (CFRTP) Tensile Test Specimens, Open Journal of Composite Materials 06 (2016) 18–27. URL: `http://www.scirp.org/journal/doi.aspx?DOI=10.4236/ojcm.2016.61003`. doi:10.4236/ojcm.2016.61003.

[11] J. Justo, L. Távara, L. García-Guzmán, F. París, Characterization of 3d printed long fibre reinforced composites, Composite Structures 185 (2018) 537–548.

[12] M. Caminero, J. Chacón, I. García-Moreno, G. Rodríguez, Impact damage resistance of 3D printed continuous fibre rein-

forced thermoplastic composites using fused deposition modelling, Composites Part B: Engineering 148 (2018) 93–103. URL: `http://linkinghub.elsevier.com/retrieve/pii/S1359836818306553`. doi:10.1016/j.compositesb.2018.04.054.

[13] M. A. Caminero, J. M. Chacón, J. M. Reverte, Interlaminar bonding performance of 3D printed continuous fibre reinforced thermoplastic composites using fused deposition modelling M.A., Polymer Testing 148 (2018) 93–103. URL: `https://doi.org/10.1016/j.polymertesting.2018.04.038`. doi:10.1016/j.polymertesting.2018.04.038.

[14] C. Pascual-González, M. Iragi, A. Fernández, J. Fernández-Blázquez, L. Aretxabaleta, C. Lopes, An approach to analyse the factors behind the micromechanical response of 3d-printed composites, Composites Part B: Engineering 186 (2020) 107820.

[15] W. Ye, G. Lin, W. Wu, P. Geng, X. Hu, Z. Gao, J. Zhao, Separated 3d printing of continuous carbon fiber reinforced thermoplastic polyimide, Composites Part A: Applied Science and Manufacturing], volume = 121, pages = 457 - 464, year = 2019, (????).

[16] J. Chacón, M. Caminero, P. Núñez, E. García-Plaza, I. García-Moreno, J. Reverte, Additive manufacturing of continuous fibre reinforced thermoplastic composites using fused deposition modelling: Effect of process parameters on mechanical properties, Composites Science and Technology 181 (2019) 107688. doi:https://doi.org/10.1016/j.compscitech.2019.107688.

[17] N. Li, G. Link, T. Wang, V. Ramopoulos, D. Neumaier, J. Hofele, M. Walter, J. Jelonnek, Path-designed 3d printing for topological optimized continuous carbon fibre reinforced composite structures, Composites Part B: Engineering 182 (2020) 107612.

[18] M. Araya-Calvo, I. López-Gómez, N. Chamberlain-Simon, J. L. León-Salazar, T. Guillén-Girón, J. S. Corrales-Cordero, O. Sánchez-Brenes, Evaluation of compressive and flexural properties of continuous fiber fabrication additive manufacturing technology, Additive Manufacturing 22 (2018) 157–164.

[19] B. Brenken, E. Barocio, A. Favaloro, V. Kunc, R. B. Pipes, Fused filament fabrication of fiber-reinforced polymers: A review, Additive Manufacturing 21 (2018) 1–16.

[20] T. A. Dutra, R. T. L. Ferreira, H. B. Resende, A. Guimarães, Mechanical characterization and asymptotic homogenization of 3d-printed continuous carbon fiber-reinforced thermoplastic, Journal of the Brazilian Society of Mechanical Sciences and Engineering 41 (2019) 133.

[21] H. Shiratori, A. Todoroki, M. Ueda, R. Matsuzaki, Y. Hirano, Compressive strength degradation of the curved sections of 3d-printed continuous carbon fiber composite, Composites Part A: Applied Science and Manufacturing (2020) 106244.

[22] W. Y. Yeong, G. D. Goh, 3d printing of carbon fiber composite: The future of composite industry?, Matter 2 (2020) 1361–1363.

[23] Y. Ma, M. Ueda, T. Yokozeki, T. Sugahara, Y. Yang, H. Hamada, A comparative study of the mechanical properties and failure behavior of carbon fiber/epoxy and carbon fiber/polyamide 6 unidirectional composites, Composite Structures 160 (2017) 89–99.

[24] M. Serna Moreno, A. Romero Gutiérrez, J. Martínez Vicente, Different response under tension and compression of unidirectional carbon fibre laminates in a three-point bending test, Composite Structures 136 (2016) 706 – 711. URL: `http://www.sciencedirect.com/science/article/pii/S0263822315004808`. doi:https://doi.org/10.1016/j.compstruct.2015.06.017.

[25] A. Smiley, R. Pipes, Rate effects on mode i interlaminar fracture toughness in composite materials, Journal of composite materials 21 (1987) 670–687.

[26] M. Iragi, C. Pascual-González, A. Esnaola, C. Lopes, L. Aretxabaleta, Ply and interlaminar behaviours of 3d printed continuous carbon fibre-reinforced thermoplastic laminates; effects of processing conditions and microstructure, Additive Manufacturing 30 (2019) 100884.

[27] H. Li, T. Wang, J. Sun, Z. Yu, The effect of process parameters in fused deposition modelling on bonding degree and mechanical properties, Rapid Prototyping Journal (2018).

[28] S. Wang, Y. Ma, Z. Deng, S. Zhang, J. Cai, Effects of fused deposition modeling process parameters on tensile, dynamic mechanical properties of 3d printed polylactic acid materials, Polymer Testing (2020) 106483.

[29] H. Zhang, J. Chen, D. Yang, Fibre misalignment and breakage in 3d printing of continuous carbon fibre reinforced thermoplastic composites, Additive Manufacturing 38 (2021) 101775. URL: `http://www.sciencedirect.com/science/article/pii/S2214860420311477`. doi:https://doi.org/10.1016/j.addma.2020.101775.

[30] J. Soete, B. Badoux, Y. Swolfs, L. Gorbatikh, et al., Defect detection in 3d printed carbon fibre composites using x-ray computed tomography, https://www. ndt. net/article/ctc2019/papers/iCT2019_Full_paper_62. pdf (2019) 1–8.

[31] H. Mei, Z. Ali, Y. Yan, I. Ali, L. Cheng, Influence of mixed isotropic fiber angles and hot press on the mechanical properties of 3d printed composites, Additive Manufacturing 27 (2019) 150–158.

[32] Q. He, H. Wang, K. Fu, L. Ye, 3d printed continuous cf/pa6 composites: Effect of microscopic voids on mechanical performance, Composites Science and Technology (2020) 108077.

[33] K. Guduru, G. Srinivasu, Effect of post treatment on tensile properties of carbon reinforced pla composite by 3d printing, Materials Today: Proceedings (2020). URL: `http://www.sciencedirect.com/science/article/pii/S2214785320319088`. doi:https://doi.org/10.1016/j.matpr.2020.03.128.

[34] M. Ueda, S. Kishimoto, M. Yamawaki, R. Matsuzaki, A. Todoroki, Y. Hirano, A. L. Duigou], 3d compaction printing of a continuous carbon fiber reinforced thermoplastic, Composites Part A: Applied Science and Manufacturing 137 (2020) 105985. URL: `http://www.sciencedirect.com/science/article/pii/S1359835X20302244`. doi:https://doi.org/10.1016/j.compositesa.2020.105985.

[35] E. A. Papon, A. Haque, S. K. Spear, Effects of functionalization and annealing in enhancing the interfacial bonding and mechanical properties of 3d printed fiber-reinforced composites, Materials Today Communications 25 (2020) 101365. URL:

`http://www.sciencedirect.com/science/article/pii/S235249282032376X`. doi:https://doi.org/10.1016/j.mtcomm.2020.101365.

[36] F. Boey, S. Lye, Void reduction in autoclave processing of thermoset composites: Part 1: High pressure effects on void reduction, Composites 23 (1992) 261–265.

[37] A. C. D.-. on Composite Materials, Standard test method for short-beam strength of polymer matrix composite materials and their laminates, ASTM International, 2006.

[38] R. Greco, L. Nicolais, Glass transition temperature in nylons, Polymer 17 (1976) 1049–1053.

[39] E. Klata, K. Van de Velde, I. Krucińska, Dsc investigations of polyamide 6 in hybrid gf/pa 6 yarns and composites, Polymer testing 22 (2003) 929–937.

[40] M. N. Islam, B. Boswell, A. Pramanik, An investigation of dimensional accuracy of parts produced by three-dimensional printing, in: Proceedings of the World Congress on Engineering 2013, IAENG, 2013, pp. 522–525.

[41] A. Farzadi, M. Solati-Hashjin, M. Asadi-Eydivand, N. A. A. Osman, Effect of layer thickness and printing orientation on mechanical properties and dimensional accuracy of 3d printed porous samples for bone tissue engineering, PloS one 9 (2014).

[42] E. Pei, G. W. Melenka, J. S. Schofield, M. R. Dawson, J. P. Carey, Evaluation of dimensional accuracy and material properties of the makerbot 3d desktop printer, Rapid Prototyping Journal (2015).

[43] G. W. Melenka, B. K. Cheung, J. S. Schofield, M. R. Dawson, J. P. Carey, Evaluation and prediction of the tensile properties of continuous fiber-reinforced 3d printed structures, Composite Structures 153 (2016) 866–875.

[44] H. Al Abadi, H.-T. Thai, V. Paton-Cole, V. Patel, Elastic properties of 3d printed fibre-reinforced structures, Composite Structures 193 (2018) 8–18.

[45] D. Saenz-Castillo, M. Martín, S. Calvo, F. Rodriguez-Lence, A. Güemes, Effect of processing parameters and void content on mechanical properties and ndi of thermoplastic composites, Composites Part A: Applied Science and Manufacturing 121 (2019) 308–320.

[46] D. Zhang, D. Heider, J. W. Gillespie Jr, Volatile removal during out of autoclave processing of high performance thermoplastic composites, CAMX-2014, Orlando, FL (2014) 13–16.

[47] C. Yang, X. Tian, T. Liu, Y. Cao, D. Li, 3d printing for continuous fiber reinforced thermoplastic composites: mechanism and performance, Rapid Prototyping Journal (2017).

[48] D. Bull, L. Helfen, I. Sinclair, S. Spearing, T. Baumbach, A comparison of multi-scale 3d x-ray tomographic inspection techniques for assessing carbon fibre composite impact damage, Composites Science and Technology 75 (2013) 55 – 61. URL: `http://www.sciencedirect.com/science/article/pii/S0266353812004137`. doi:https://doi.org/10.1016/j.compscitech.2012.12.006.

[49] C. Kousiatza, D. Tzetzis, D. Karalekas, In-situ characterization of 3d printed continuous fiber reinforced composites: A methodological study using fiber bragg grating sensors, Composites Science and Technology 174 (2019) 134 – 141. URL: `http://www.sciencedirect.com/science/article/pii/S0266353818329075`. doi:https://doi.org/10.1016/j.compscitech.2019.02.008.

[50] D. Prevorsek, R. Butler, H. Reimschuessel, Mechanical relaxations in polyamides, Journal of Polymer Science Part A-2: Polymer Physics 9 (1971) 867–886.

[51] J. Pagacz, K. N. Raftopoulos, A. Leszczyńska, K. Pielichowski, Biopolyamides based on renewable raw materials, Journal of Thermal Analysis and Calorimetry 123 (2016) 1225–1237.

[52] A. R. O. de Figueiredo Martins, Effect of intermolecular interactions on the viscoelastic behavior of polyamides, Ph.D. thesis, 2019.

[53] R. H. Boyd, Dielectric loss in 66 nylon (polyhexamethylene adipamide), The Journal of Chemical Physics 30 (1959) 1276–1283.

[54] T. Kawaguchi, The dynamic mechanical properties of nylons, Journal of Applied Polymer Science 2 (1959) 56–61.

[55] K. Pramoda, T. Liu, Effect of moisture on the dynamic mechanical relaxation of polyamide-6/clay nanocomposites, Journal of Polymer Science Part B: Polymer Physics 42 (2004) 1823–1830.

[56] T. Tsutsui, R. Tanaka, T. Tanaka, Mechanical relaxations in some ionene polymers. ii. influence of counterions and absorbed water, Journal of Polymer Science: Polymer Physics Edition 14 (1976) 2273–2284.

[57] W. Stark, M. Jaunich, J. McHugh, Carbon-fibre epoxy prepreg (cfc) curing in an autoclave analogue process controlled by dynamic mechanical analysis (dma), Polymer testing 32 (2013) 1487–1494.

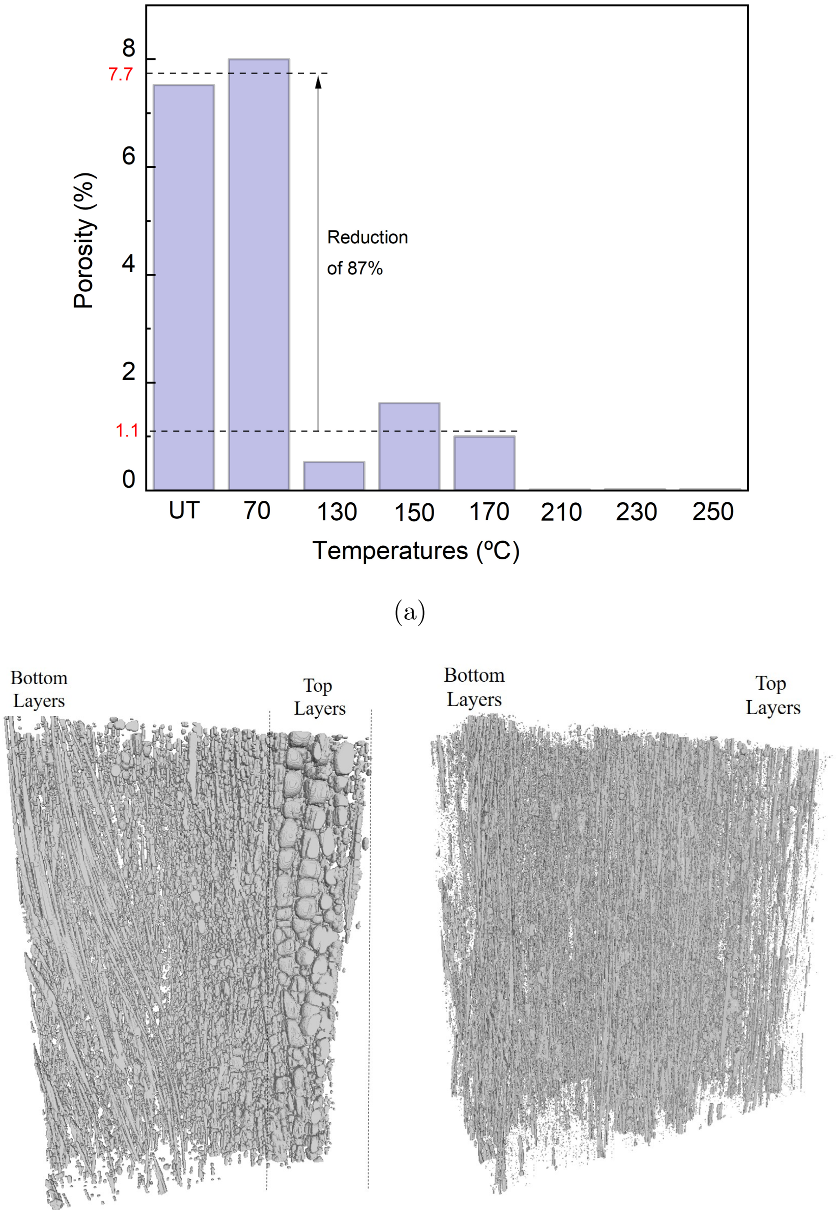

(a)

(b)

(c)

Figure 5: (a) Evolution of porosity content with temperature post-processing. Front view of reconstructed 3D images of the extracted porosity for printed unidirectional CCFRC coupons treated at (b) 70°C and (c) 150°C from X-ray computed tomography data. First and last layers to be deposited during printing are indicated as bottom and top layers in the images.

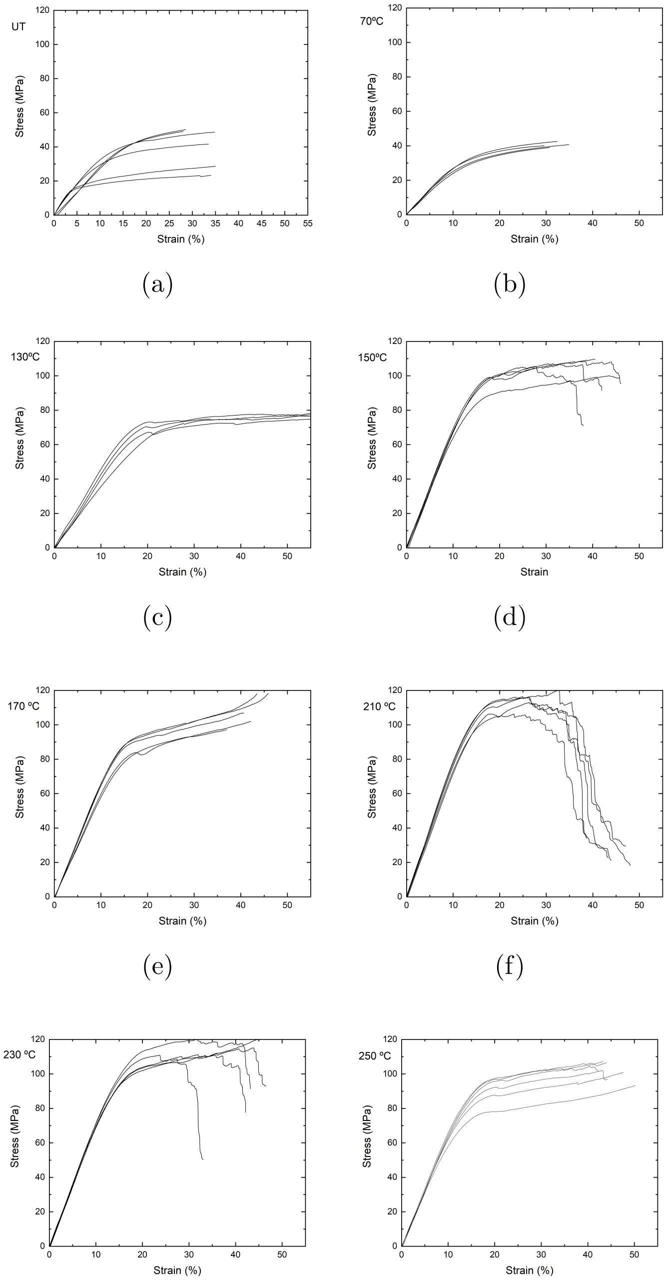

(a) (b)

(c) (d)

(e) (f)

(g) (h)

Figure 6: Stress–strain curves of the short-beam shear test of printed unidirectional CCFRC coupons (a) untreated and treated (b) at 70°C, (c) at 130°C, (d) at 150°C, (e) at 170°C, (f) at 210°C, (g) at 230°C and (h) at 250°C.

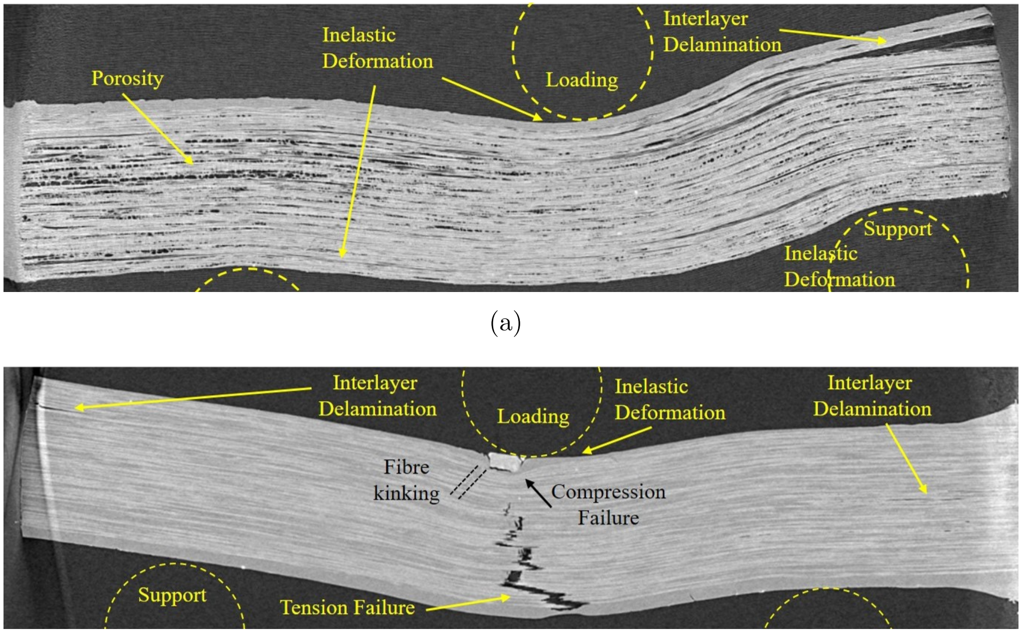

(a)

(b)

Figure 7: X-CT images of failure modes after short-beam shear test for unidirectional CCFRC coupons treated (a) at 70°C and (b) 150°C.

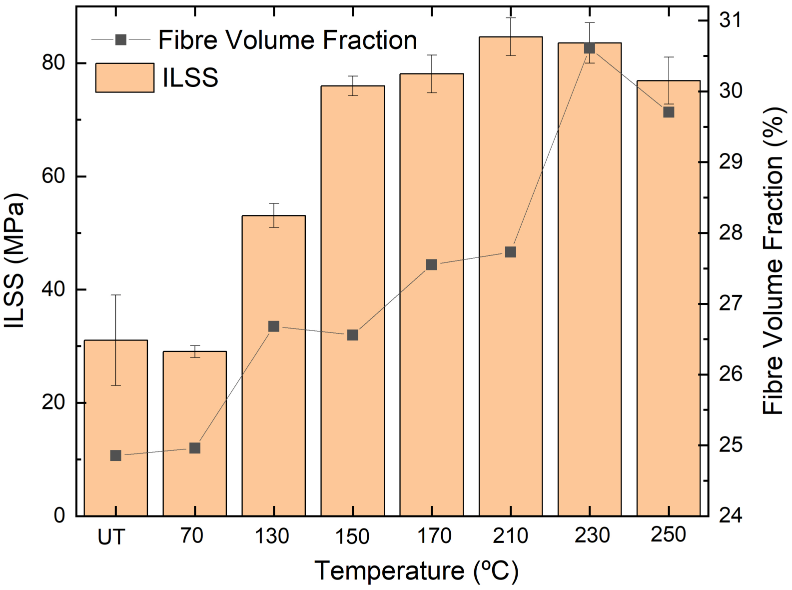

Figure 8: ILSS and fibre volume fraction evolution as function of post-processing temperatures.

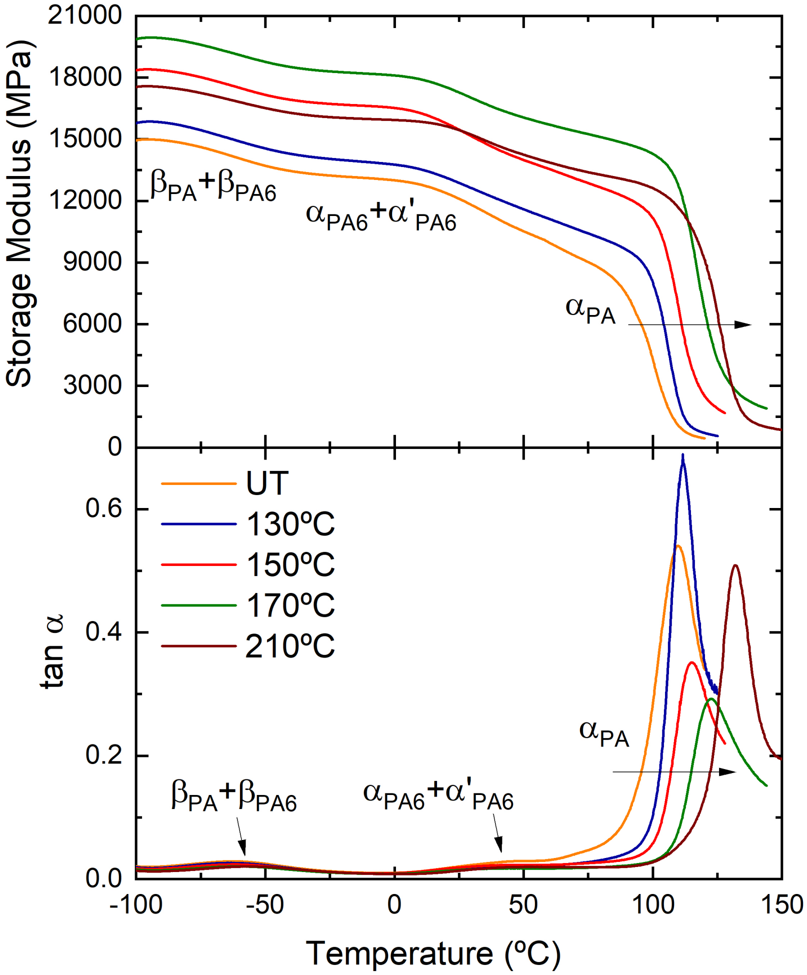

Figure 9: Storage modulus and tanα curves for unidirectional CCFRC coupons post-processed at 70°C, at 150°C, at 170°C and at 210°C.

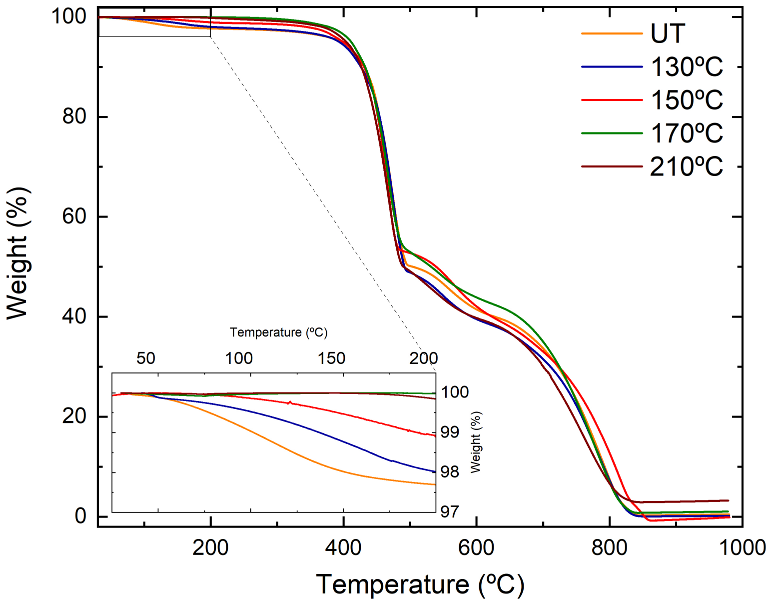

Figure 10: TGA curves of unidirectional CCFRC coupons untreated (UT) and treated at 70°C, at 150°C, at 170°C and at 210°C. Inset graph: closer inspection of the weight loss between room temperature and 200°C, corresponding to evaporation of water.

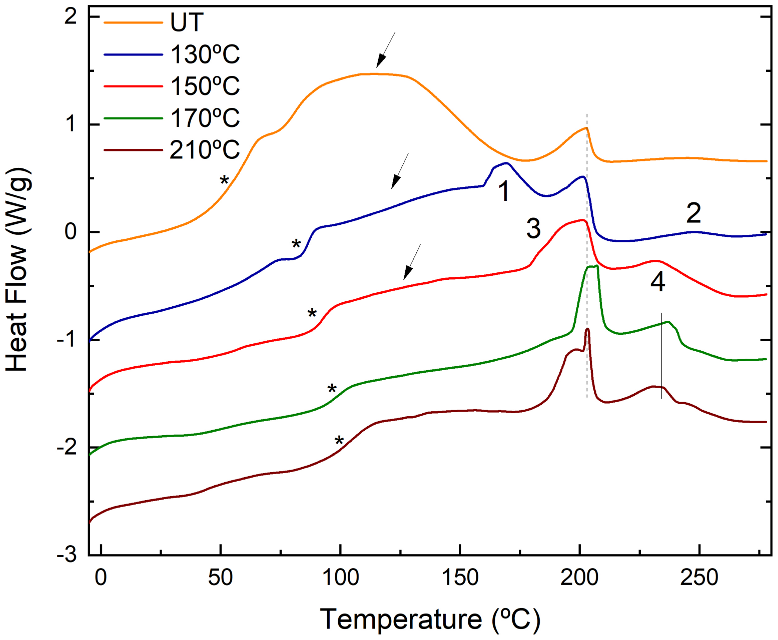

Figure 11: DSC curves for heating cycle applied to unidirectional CCFRC coupons untreated (UT) and treated at 70°C, at 150°C, at 170°C and at 210°C. Scanning rate: 10°C /min. Upon post-processing temperature, new peaks emerge at lower (named as 1 and 3) and higher temperatures (indicated as 2, 4 and the continuous line).